Measuring the Charge of a Single Dielectric Nanoparticle Using a High-Q Optical Microresonator

You-Ling Chen,[1] Wei-Liang Jin,[2,3] Yun-Feng Xiao,[2] and Xuming Zhang[1,*]

[1]*Department of Applied Physics, The Hong Kong Polytechnic University, Hong Kong SAR 999077, People's Republic of China*

[2]*State Key Lab for Mesoscopic Physics and Department of Physics, Peking University, Beijing 100871, People's Republic of China*

[3]*Department of Electrical Engineering, Princeton University, Princeton, New Jersey 08544, USA*

(Received 18 May 2016; revised manuscript received 5 October 2016; published 28 October 2016)

Measuring the charge of a nanoparticle is of great importance in many fields including optics, astronomy, biochemistry, atmospheric science, environmental engineering, and dusty plasma. Here, we propose to use a high-Q whispering-gallery-mode (WGM) optical microresonator to detect the surface and bulk charge of a dielectric nanoparticle. Because of the modification of nanoparticle conductivity induced by the surplus electrons, both the coupling strength between the nanoparticle and the WGM and the dissipation changes compared with the case of a neutral nanoparticle. The charge density can be inferred from the transmission spectrum of the WGM microresonator. By monitoring the mode splitting, the linewidth broadening or the resonance dip value of the transmission spectrum, surface (bulk) electron density as low as 0.007 nm^{-2} (0.001 nm^{-3}) can be detected for nanoparticles with negative (positive) electron affinity. The high sensitivity is attributed to the ultranarrow resonance linewidth and small mode volume of the microresonator.

DOI: 10.1103/PhysRevApplied.6.044021

I. INTRODUCTION

Over the past few years, optical whispering-gallery-mode (WGM) microresonators including microspheres [1–3], microrings [4–8], microtoroids [9–12], microbubbles [13–15], and microtubes [16,17] have become valuable tools in sensing applications due to the significantly enhanced light-matter interaction provided by their ultrahigh-Q factors and small mode volumes [18,19]. So far, by monitoring either the cavity-resonant wavelength shift (mode shift) [20–26] or mode splitting [27–30], single nanoparticle binding events have been resolved. The former sensing scheme has a large detection range in particle size, while the latter is immune to various noises such as environmental temperature drift. Recently, by employing the mode-broadening mechanism, Refs. [31,32] reported the detection of individual polystyrene nanoparticles and lentiviruses. In the above-mentioned WGM microresonator sensors, the sensing signal corresponds to either the size or the permittivity of particles. However, WGM microcavity-based nanoparticle charge measurement remains unstudied.

Many particles in nature are, however, not neutral but charged in the fields of astronomy, dusty plasma, atmospheric sciences, manufacture of integrated circuit, environmental engineering, surface chemistry, and biochemical engineering [33–38]. For example, grains in supernova shells, red giant photospheres, and noctilucent clouds are highly charged. In recent years, air pollution has become a severe threat to human health. The main pollution sources, including industrial dusts and chemical colloids suspended in air, are also charged. Nanoparticle charge is a crucial parameter in optics: it not only attracts theoretical studies on the differed electromagnetic field scattering pattern compared to neutral nanoparticles [39–46], but it also is applied to enhance light absorption [47,48], Raman scattering [49], molecular fluorescence [50], and even to help manipulate nanoparticles [51]. To measure the charge, traditional electrical methods [34,52–54] are limited to micron-sized particles. For particles with even smaller size, optical measurement is a better choice, as excess electrons affect light scattering. However, even for highly charged nanoparticles, the optical method is also challenging because the influence on light scattering caused by surplus electrons is negligible. Various enhancements are implemented, such as the anomalous resonance [42–44] and the surface plasmon resonance [48], yet the detection resolution is still limited due to the large resonance linewidth.

In this paper, we propose to use the high-Q WGM optical resonator to measure the charge of a nanoparticle. A single nanoparticle adsorbed to the resonator results in mode splitting of the two initially degenerate whispering gallery modes through backscattering. Because of the modification of nanoparticle conductivity induced by the surplus electrons, both the nanoparticle-WGM coupling strength and the dissipation changes accordingly compared with the case of a neutral nanoparticle. The charge density of the

*apzhang@polyu.edu.hk

nanoparticle can be inferred by monitoring the mode splitting, the linewidth broadening, or the resonance dip value of the transmission spectrum of the microcavity. Because of the ultranarrow resonance linewidth and small mode volume of the microresonator, measurement of surface and bulk charge with very low charge density is realized.

II. THEORETICAL MODEL OF THE SENSING SCHEME

The sensing system is illustrated in Fig. 1. A tunable pump laser at a wavelength band of 1550 nm is launched from a tapered fiber to excite the whispering gallery modes of a silica microsphere in air through evanescent coupling. The transmitted light is monitored through a low-noise photodetector connected to an oscilloscope. Comparing the transmission spectrum induced by a charged nanoparticle with that induced by a neutral nanoparticle of all other parameters the same, we can infer the information of the charge.

Before proceeding to the charged nanoparticle case, here we briefly review the detection of an uncharged particle through the mode-splitting mechanism [55–59] of a WGM microresonator. For a perfect WGM microsphere, its eigenmodes are twofold degenerate with identical resonance frequency and linewidth: the clockwise (CW) and counterclockwise (CCW) propagating modes. When a subwavelength scatterer enters the mode volume, the backscattering of the WGM field couples the CW and CCW modes. As a result, the originally degenerate mode splits into two new orthogonal standing modes with different resonance frequencies and linewidths: the symmetric mode and the antisymmetric mode, and the degeneracy is lifted. Consequently, the transmission spectrum of the fiber taper behaves as a doublet, as shown in Fig. 1.

Next, we proceed to the case of a charged dielectric nanoparticle. While a dielectric nanoparticle exhibits

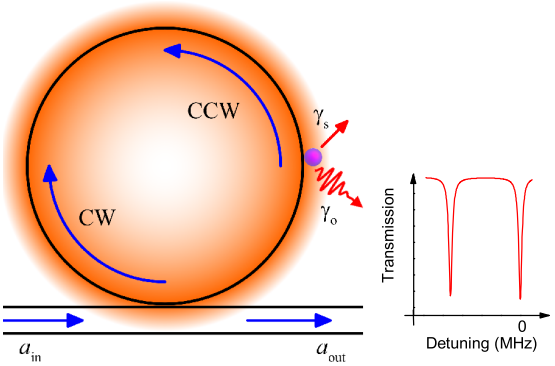

FIG. 1. Schematic illustration of a WGM microresonator with a charged nanoparticle attached to its surface. γ_s is the Rayleigh scattering loss, and γ_0 represents the Ohmic loss. CW and CCW are the clockwise and counterclockwise propagating modes. The typical fiber taper transmission spectrum behaves as a doublet.

perfect insulator properties, surplus electrons will introduce a nonzero electric conductivity. Unlike metal, the conductivity is small due to the strong confinement by electron-phonon interactions. The charged nanoparticle can be classified into two main categories according to the electron affinity χ [42]. For particles with $\chi < 0$, such as MgO, LiF, and CaO, the conduction-band minimum inside the dielectric lies above the surface potential outside the particle. In this case, the surplus electrons are trapped in the image potential induced by the transverse optical phonon in the surface [60] instead of penetrating into the particle [61]. At room temperature, the de Broglie wavelength of the surface electron is about 10 nm. As a result, for particles with radius $r > 10$ nm, the surface can be approximated as a plane surface, and the contribution from surplus electrons can be encoded as extra surface conductivity c_s. For particles with $\chi > 0$, such as Cu_2O, Al_2O_3, and PbS, the surface potential lies above the conduction band, and extra electrons are confined in the conduction band by the longitudinal optical bulk phonon [60]. The conduction band lies homogeneously throughout the particle for a micron-sized or even smaller particle. In this case, the contribution from surplus electrons can be treated as extra bulk conductivity c_b. Within the memory function approach [62], the surface and bulk conductivity can be expressed by

$$c_{s(b)} = \frac{e^2 n_{s(b)}}{m_{s(b)}} \frac{i}{\omega + M_{s(b)}(\omega)}, \tag{1}$$

where e is the elementary charge, $n_s(n_b)$ denotes the surface (bulk) electron density, m_s and m_b are the electron mass and the conduction-band effective mass, ω denotes the frequency, and $M_s(\omega)[M_b(\omega)]$ represents the corresponding memory function.

The Mie scattering theory [63] is appropriate for studying the light scattering of a charged sphere with modified Mie coefficients [39]. For nanoparticles with $\chi < 0$, the surface charge can be treated as a coating layer. In the quasistatic limit, the effective-medium theory [48] can be used to describe the scattering effect where the surface-charged nanoparticle is approved to be equal to a neutral absorbing nanoparticle with the same size but different permittivity. The additional effective permittivity can be expressed by

$$\Delta\varepsilon = i\frac{2}{r}\frac{c_s}{\omega}. \tag{2}$$

For nanoparticles with $\chi > 0$, straightforwardly we can obtain

$$\Delta\varepsilon = i\frac{c_b}{\omega}. \tag{3}$$

The nanoparticle total effective permittivity can be expressed as $\tilde{\varepsilon} = \varepsilon_0 + \Delta\varepsilon$, with ε_0 being the permittivity for the neutral material. With the material parameters listed

TABLE I. Calculated nanoparticle effective permittivity change induced by surplus electrons. The wavelength of the incident laser is 1550 nm, and the nanoparticle radius $r = 40$ nm. n_e is the electron density, whose unit is nm^{-2} for $\chi < 0$, and nm^{-3} for $\chi > 0$. $\Delta\varepsilon$ is the charge-induced additional permittivity and $\tilde{\varepsilon}$ denotes the total permittivity.

Material	χ	n_e	$\Delta\varepsilon$	$\tilde{\varepsilon}$
MgO	<0	0.3	$-0.0072 + 0.0134i$	$2.9329 + 0.0134i$
LiF	<0	0.3	$-0.0042 + 0.0108i$	$1.9078 + 0.0108i$
PbS	>0	0.03	$-0.3678 + 0.0016i$	$17.6503 + 0.0016i$
Al_2O_3	>0	0.03	$-0.1605 + 0.0078i$	$2.8880 + 0.0078i$
Cu_2O	>0	0.03	$-0.1149 + 0.0004i$	$6.4860 + 0.0004i$

in Ref. [43], we have calculated $\Delta\varepsilon$ for five nanoparticles including MgO, LiF ($\chi < 0$) and PbS, Cu_2O, Al_2O_3 ($\chi > 0$), where the wavelength of the incident laser is 1550 nm and $r = 40$ nm, as shown in Table I. In the last column, we approximate the five uncharged materials to be good insulators at such a wavelength band. From the total permittivity column in Table I, it is not difficult to find out that neither anomalous scattering nor surface plasmon resonance is possible to occur for such an incident laser wavelength. For example, anomalous scattering occurs at frequencies where Re $[\tilde{\varepsilon}] < 0$ and Im $[\tilde{\varepsilon}] \ll 1$. Moreover, $\Delta\varepsilon$ is small, making the charge-induced local permittivity difference difficult to be resolved. However, whispering-gallery-mode microcavity is an ideal candidate to measure the nanoparticle charge as it is able to detect small local refractive-index fluctuations.

We have also calculated $\Delta\varepsilon$ under different surface and bulk electron densities for a MgO and Cu_2O nanoparticle, as shown in Fig. 2. We can find that regardless of materials with $\chi > 0$ or $\chi < 0$, Re $[\Delta\varepsilon]$ and Im $[\Delta\varepsilon]$ are proportional to the surface and bulk electron density. For materials with $\chi < 0$, $|\mathrm{Re}[\Delta\varepsilon]| < |\mathrm{Im}[\Delta\varepsilon]|$; while for materials with $\chi > 0$, $|\mathrm{Re}[\Delta\varepsilon]| \gg |\mathrm{Im}[\Delta\varepsilon]|$.

Next, we study the charge-induced transmission spectrum change. A nanoparticle with radius $r \ll \lambda$ can be treated as a Rayleigh scatterer with complex polarizability

$$\tilde{\alpha} = 4\pi r^3(\tilde{\varepsilon} - 1)/(\tilde{\varepsilon} + 2). \tag{4}$$

The total Hamiltonian contains three parts: the free Hamiltonian of the WGMs and the reservoir, H_0; the nanoparticle-induced scattering into the same or counter-propagating cavity mode, H_1; and the nanoparticle-induced scattering into the reservoir modes, H_2. As the nanoparticle radius $r \ll \lambda$, Weisskopf-Wigner semi-QED treatment [28] is appropriate to solve the interaction between the WGMs and the nanoparticle. The Hamiltonian can be written as

$$H = H_0 + H_1 + H_2, \tag{5}$$

$$H_0 = \sum_{m=\mathrm{CW,CCW}} \hbar\omega_c a_m^+ a_m + \sum_j \hbar\omega_j b_j^+ b_j, \tag{6}$$

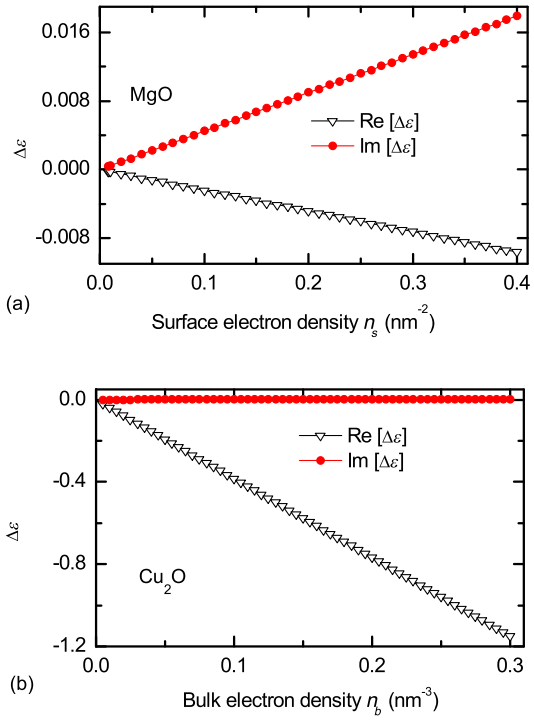

FIG. 2. (a) The additional complex permittivity $\Delta\varepsilon$ for a MgO nanoparticle under different surface electron densities. (b) $\Delta\varepsilon$ for a Cu_2O nanoparticle under different bulk electron densities. Other parameters: $\lambda = 1550$ nm, $r = 40$ nm.

$$H_1 = \sum_{m,m'=\mathrm{CW,CCW}} \hbar\tilde{g}_{m,m'} a_m^+ a_{m'}, \tag{7}$$

$$H_2 = \sum_{m=\mathrm{CW,CCW}} \sum_j \hbar\tilde{g}_{m,j}(b_j^+ a_m + \mathrm{H.c.}), \tag{8}$$

where ω_c is the degenerate frequency of the CW and CCW WGMs, ω_j represents the frequency of the j reservoir mode, a_m^+, b_j^+ (a_m, b_j) are the creation (annihilation) operators of the m resonator mode, and the j reservoir mode, respectively. $\tilde{g}_{m,m'}$ ($\tilde{g}_{m,j}$) is the complex coupling coefficient between the m WGM mode and the m' WGM mode (j reservoir mode). Within dipole approximation [28,64], the complex coupling coefficient

$$\tilde{g}_{m,m'} = -\frac{\tilde{\alpha} f^2(\vec{r})\omega_c}{2V_m} = \tilde{g}_1 + i\tilde{g}_2, \tag{9}$$

where $f(\vec{r})$ represents the normalized WGM field magnitude at the nanoparticle position $\vec{r}$, V_m denotes the cavity mode volume, and $\tilde{g}_1$ and $\tilde{g}_2$ are the real and imaginary part of $\tilde{g}_{m,m'}$. Following the Heisenberg equation of motion and the established Weisskopf-Wigner derivation, we finally arrive at the following formalism:

$$\frac{da_m}{dt} = -\left[i(\omega_c + \tilde{g}_1) + \frac{\gamma_s' + \kappa_0 + \kappa_1}{2}\right] a_m - \left(i\tilde{g}_1 + \frac{\gamma_s'}{2}\right) a_{m'\neq m} - \sqrt{\kappa_1} a_m^{\text{in}}, \tag{10}$$

where κ_0, κ_1, and a_m^{in} are the intrinsic damping rate of the m cavity mode, the taper-cavity coupling rate, and the input field. The new decay rate $\gamma_s' = \gamma_s - 2\tilde{g}_2$, where $\gamma_s = [|\tilde{\alpha}|^2 f^2(\vec{r})\omega_c^4/(6\pi c^3 V_m)]$. Compared with the neutral nanoparticle case, the formalism is almost the same, except that the coupling strength is modified from g to $\tilde{g}_1$, and the total decay rate changes from γ_s to γ_s'.

To understand the decay terms in the above equation, we start from classical electrodynamics, where the scattering and absorption cross sections of a sphere are $\sigma_s = [|\tilde{\alpha}|^2/(6\pi)](\omega^4/c^4)$ and $\sigma_0 = (\omega/c)\text{Im}[\tilde{\alpha}]$, respectively. By considering the total lost power with $I_{\text{inc}}\sigma = \hbar\omega_c\Gamma$, where $I_{\text{inc}} = [\hbar\omega_c c/(V_m)]$ denotes the incident field intensity, the total decay rate Γ can be divided into two parts: the scattering-induced decay $\Gamma_s = [|\tilde{\alpha}|^2 f^2(\vec{r})\omega_c^4/(6\pi c^3 V_m)]$ and the absorption-induced decay $\Gamma_0 = [\omega_c \text{Im}[\tilde{\alpha}]/(V_m)]f^2(\vec{r})$. It can be found that $\Gamma_s = \gamma_s$ and $\Gamma_0 = -2\tilde{g}_2$. In other words, the total decay rate γ_s' consists of Rayleigh scattering into vacuum and the Ohmic dissipation. In the following, we denote the Ohmic loss as γ_0.

With the standard input-output relation, we can obtain the transmission spectrum collected from the taper

$$T = \left|1 - \frac{\kappa_1}{2}\sum_{q=+,-}\frac{1}{i(-\Delta + g_q) + (\kappa_0 + \kappa_1 + \Gamma_q)/2}\right|^2, \tag{11}$$

where $\Delta = \omega - \omega_c$ is the detuning, $g_+ = 0$ and $g_- = 2\tilde{g}_1$ are the resonance frequency shifts of the two new eigenmodes, and $\Gamma_+ = 0$ and $\Gamma_- = 2(\gamma_s + \gamma_0)$ denote the linewidth broadenings of the two new eigenmodes.

The surplus charge affects both the mode splitting and the linewidth broadening of the transmission spectrum. Comparing the cases of a neutral and a charged nanoparticle with the same size, dielectric constant, and binding position, the mode splitting of the two new eigenmodes changes from $|2g|$ to $|2\tilde{g}_1|$, and the linewidth broadening of the symmetric mode changes from $2\gamma_s$ to $2(\gamma_s - 2\tilde{g}_2)$. As a result, the density of surplus charge can be inferred from the transmission spectrum of the microcavity.

III. CHARGE-INDUCED CHANGE OF THE TRANSMISSION SPECTRA

A. Materials with $\chi < 0$

We compare the transmission spectrum of a WGM sphere with a single binding neutral (red solid line) and charged MgO/LiF nanoparticle (black dashed line), as shown in Figs. 3(a) and 3(c). Throughout the manuscript, we set the silica WGM sphere radius $R = 15$ μm and the wavelength $\lambda = 1550$ nm unless specified. Comparing the dashed line to the solid line, we can observe an obvious increase of the transmitted light intensity at the symmetric mode's resonant frequency, but no mode-splitting change. As shown in Table I, for $\chi < 0$ materials, the charge-induced $\Delta\varepsilon$ is dominated by the imaginary part, indicating a dominant linewidth broadening effect at the symmetric mode when extra electrons are introduced. The transmission at the eigenmode frequency, which we denote as the dip value with intensity D, characterizes the relative linewidth broadening well [65]. In the case when the mode splitting is much larger than the linewidth, the dip value for the symmetric mode is approximated as $D = [\kappa_0 + 2(\gamma_s + \gamma_0)]^2/[\kappa_0 + \kappa_1 + 2(\gamma_s + \gamma_0)]^2$. In our system, for a $r = 40$ nm nanoparticle and WGM cavity $Q \sim 10^8$, mode splitting $|2g| \sim 100$ MHz, while the linewidth $\Gamma \sim 0.1$ MHz, and so the dip-value approximation is valid. The transmission spectrum around the symmetric resonance frequency can be regarded as a single Lorentzian shape. The visible increased dip value reveals that Ohmic loss is comparable to the Rayleigh scattering loss and the cavity intrinsic loss.

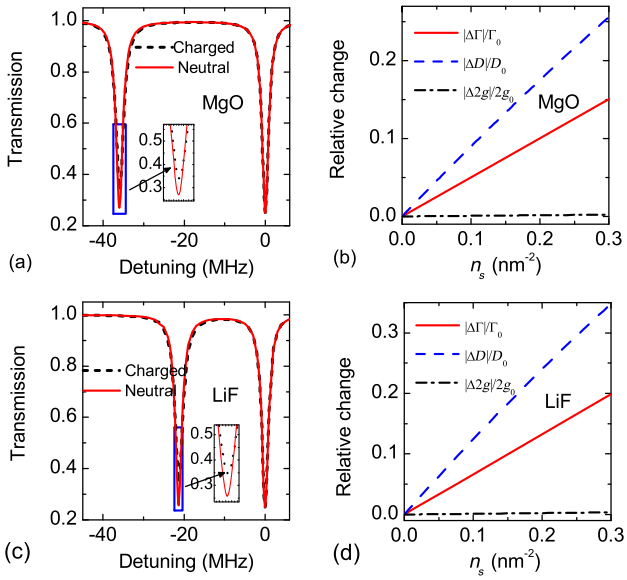

FIG. 3. (a),(c) Transmission spectrum for a WGM microcavity with a single attached neutral (red solid line) and charged MgO/LiF nanoparticle (black dashed line). The surface electron density $n_s = 0.3$ nm^{-2}. (b),(d) The MgO/LiF nanoparticle surplus charge-induced relative change of symmetric mode's linewidth (red solid line), dip value (blue dashed line), and mode splitting (black dash-dotted line) with respect to the neutral case. Other parameters: the nanoparticle radius $r = 40$ nm, the silica WGM sphere $Q \sim 10^8$, and the decay ratio $\kappa_1/\kappa_0 = 1$. The surrounding medium is supposed to be air. For other environmental conditions, the corresponding permittivity can be changed accordingly.

We quantitatively show the relative change of the symmetric mode's linewidth (solid line), dip value (dashed

line), and the mode splitting (dash-dotted line) with respect to the neutral case in Figs. 3(b) and 3(d). It should be noticed that no matter for MgO or LiF nanoparticle, though the symmetric mode is influenced obviously by surplus charge, the asymmetric mode is not affected at all. The reason is that the asymmetric mode lies at the wave node where the electromagnetic field strength is zero, while the symmetric mode lies at the wave antinode. Indeed, the slopes of the solid line and dashed line are far greater than that of the dash-dotted line. For example, for a charged MgO nanoparticle, the relative change of the dip value and the symmetric mode's linewidth can be as high as 26% and 15%, respectively, yet the relative mode-splitting change is negligible, when the surface electron density is 0.3 nm^{-2}. As a result, we can first use the mode splitting to determine the nanoparticle size, then utilize the linewidth or dip-value difference to measure the charge.

In the following, we discuss the detection limit by using the Fisher information theory [66]. The sensing system is swept-frequency based and consideration should be given to two dominant noise sources: the technical Gaussian detector noise σ_d and the fundamental thermorefractive noise σ_t [67,68]. Experimentally, when the laser frequency ω is tuned close to the WGM microcavity symmetric mode resonant frequency ω_0 (with linewidth Γ and transmission dip value D_0), discrete samples are taken at a fixed frequency interval $\Delta\Omega = \beta\Gamma$ in a finite spectral range $\Omega = W\Gamma$, where β and W are the corresponding coefficients. There are three signals of the symmetric mode which could be detected in our system: the frequency shift, the linewidth broadening, and the dip-value change. Correspondingly, the parameter vector $\vec{T} = (\omega_0, \Gamma, D_0)$. According to the Fisher information theory, $(\Delta T_i)^2 \geq 1/[F_T]_{ii}$, with ΔT_i being the detectable parameter change and $[F_T]_{ii}$ being the ith diagonal element of the Fisher information matrix corresponding to the parameter vector $\vec{T}$. Taking the Gaussian detector noise σ_d as an example, the minimum detectable dip-value change ΔD_d is calculated to be

$$\Delta D_d = 2\sqrt{\frac{\beta}{\pi}}\frac{\sigma_d}{I_0}. \tag{12}$$

In the above expression, I_0 denotes the incident laser power. Experimental parameters can be $\beta = 10^{-3}$, $\sigma_d = I_0/5$. As a result, the smallest transmission dip-value change which can be detected is $\Delta D_d = 0.007$. Similarly, the minimum detectable linewidth change $\Delta\Gamma_d$ and mode-shift change $\Delta\omega_d$ are

$$\Delta\Gamma_d = 2\Delta\omega_d = 2\sqrt{\frac{2\beta}{\pi}}\frac{\sigma_d\Gamma}{I_0 D_0}. \tag{13}$$

Unlike ΔD_d, which is determined once β and σ_d are given, $\Delta\Gamma_d$ and $\Delta\omega_d$ are also dependent on the original linewidth Γ and dip value D_0. The thermorefractive noise-limited minimum detectable parameters $\Delta\Gamma_t$, $\Delta\omega_t$, and ΔD_t can also be calculated based on the Fisher information theory. The results show that for our case $\Delta D_d \gg \Delta D_t$ and $\Delta\Gamma_d \gg \Delta\Gamma_t$. Consequently, it is reasonable that we only consider the Gaussian detector noise.

During the above analysis we have set the ratio $\kappa_1/\kappa_0 = 1$, cavity quality factor $Q = 10^8$, and nanoparticle radius $r = 40$ nm. Next, we discuss the optimization of the detection limit through these parameters. For simplicity, we take the case of a charged MgO nanoparticle as an example. The case of a LiF nanoparticle is similar.

First, we study the detection limit under different values of κ_1/κ_0. We denote the minimum detectable surface charge density n_s based on the dip-value (linewidth) change as n_{sD} ($n_{s\Gamma}$). From Fig. 3(b) we can find that both $\Delta D/D_0$ and $\Delta\Gamma/\Gamma_0$ changes approximately linearly with n_s. Suppose $\Delta D/D_0 = k_d n_s$ and $\Delta\Gamma/\Gamma_0 = k_\Gamma n_s$ with k_d and k_Γ being the corresponding slopes. In Fig. 3(b), k_d is obviously larger than k_Γ, and so the detection limit should be n_{sD}. However, with the decrease of κ_1/κ_0, k_d decreases dramatically while k_Γ keeps a constant, as shown in Fig. 4(a). We show the simulated results of n_{sD} and $n_{s\Gamma}$ in Fig. 4(b). With the increase of κ_1/κ_0, $n_{s\Gamma}$ increases while n_{sD} first decreases dramatically and then increases slightly. As a result, the detection limit should be dip-value based for large κ_1/κ_0, and linewidth based for small κ_1/κ_0. To explain the influence of κ_1/κ_0, we plot the original dip value D_0 of the neutral nanoparticle case and the corresponding slope k_d in the inset of Fig. 4(b). Based on Eqs. (12) and (13), the detection limits

$$n_{sD} = 2\sqrt{\frac{\beta}{\pi}}\frac{\sigma_d}{I_0 D_0 k_d}, \tag{14}$$

$$n_{s\Gamma} = 2\sqrt{\frac{2\beta}{\pi}}\frac{\sigma_d}{I_0 D_0 k_\Gamma}. \tag{15}$$

With the increase of κ_1/κ_0, D_0 decreases, k_d increases while k_Γ keeps a constant. As a result, n_{sD} first decreases intensively and then increases slightly due to the tradeoff between D_0 and k_d. The optimal ratio of κ_1/κ_0 is around 1.0. $n_{s\Gamma}$ increases monotonically with κ_1/κ_0. As a conclusion, the detection limit should be linewidth based for very small κ_1/κ_0, while it should be dip-value based for relatively larger κ_1/κ_0. Both n_{sD} and $n_{s\Gamma}$ can reach 0.02 nm^{-2} for $Q = 10^8$ through the optimization of κ_1/κ_0. The minimum detectable n_s can be kept below 0.04 nm^{-2} in a wide κ_1/κ_0 range.

Next, we discuss the influence of the cavity Q factor and the nanoparticle radius on the detection limit. Figure 5(a) shows the minimum detectable n_s at different cavity Q factors range from $Q = 10^7$ to $Q = 10^9$ for a MgO nanoparticle. The higher Q is, the lower the detection limit that can be achieved. For example, the minimum detectable n_s corresponding to Q factors of 5×10^8, 1×10^8, and 1×10^7 are 0.007 nm^{-2}, 0.028 nm^{-2}, and 0.294 nm^{-2}. Detection

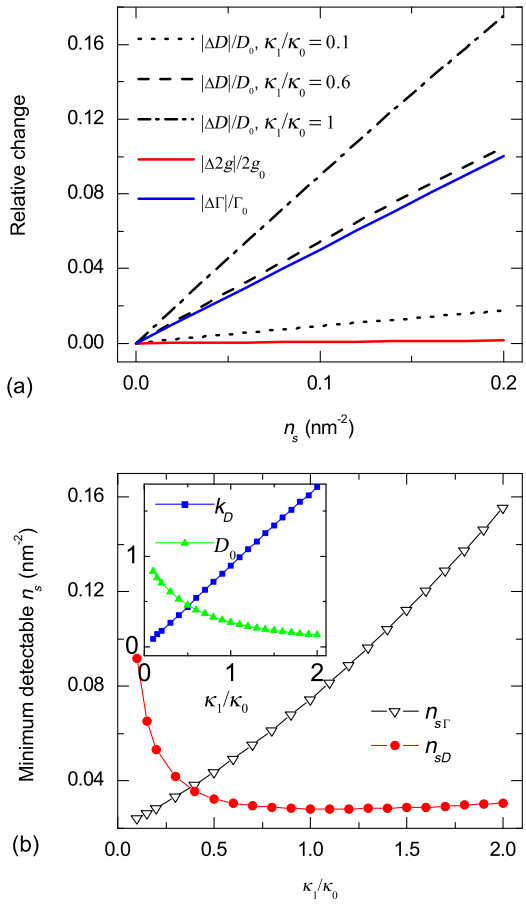

FIG. 4. (a) The relative change of symmetric mode's linewidth, dip value, and mode splitting with n_s at different values of κ_1/κ_0. (b) The minimum detectable n_s based on linewidth and dip-value detection with the increase of κ_1/κ_0. Inset: the original dip value and the slope of $|\Delta D|/D_0$ for a neutral nanoparticle with κ_1/κ_0. Other parameters: MgO nanoparticle radius $r = 40$ nm, cavity $Q = 10^8$.

limit as low as $n_s = 0.004$ nm^{-2} is achieved when $Q = 10^9$. From Fig. 5(b) we can find that for a very small MgO nanoparticle, it is reasonable to choose the dip value as the sensing signal; while for a larger MgO nanoparticle, the change of linewidth is more sensitive.

B. Materials with $\chi > 0$

For materials with $\chi > 0$ such as PbS, Cu_2O, and Al_2O_3, however, as shown in Table I, the charge-induced $\Delta\varepsilon$ is dominated by the real part, indicating a dominant mode-splitting change effect. In Figs. 6(a) and 6(c) we compare the transmission spectrum for a WGM sphere with a single binding Cu_2O/PbS nanoparticle without charge (red solid line) and with charge (black dashed line). As predicted, we can observe an obvious decrease of mode splitting, but negligible dip-value change. This result is also quantitatively demonstrated in Figs. 6(b) and 6(d), where the relative change of symmetric mode's linewidth (red solid

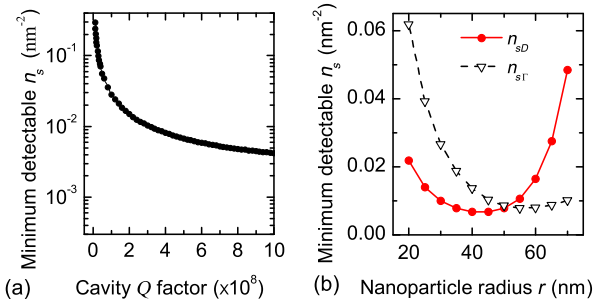

FIG. 5. Minimum detectable n_s of MgO nanoparticle at different (a) cavity Q factors (nanoparticle radius $r = 40$ nm). (b) nanoparticle radii (cavity $Q \sim 5 \times 10^8$). The red solid curve and the black dashed curve correspond to the dip-value-based and linewidth-based detection limits, respectively. $\kappa_1/\kappa_0 = 1.0$.

line), dip value (blue dashed line), and mode splitting (black dash-dotted line) are calculated with respect to the bulk electron density n_b. The slope of the mode splitting is obviously larger than that of the other two lines. As a result, we can first use the dip value or the linewidth to determine the nanoparticle size, and then utilize the mode-splitting difference to measure the charge.

The detection limit can also be calculated using the Fisher information theory. Here, we discuss the result for a

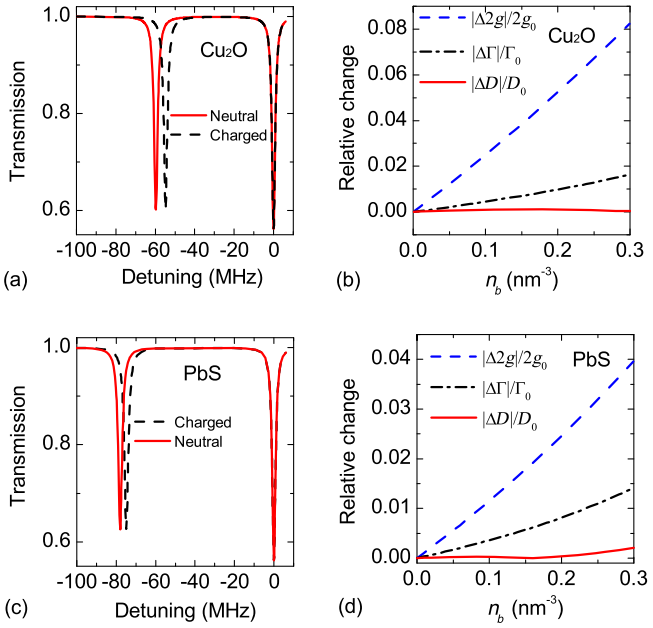

FIG. 6. (a),(c) Transmission spectrum for a WGM microcavity with a single deposited Cu_2O/PbS nanoparticle without charge (red solid line) and with charge (black dashed line). The bulk electron density $n_b = 0.3$ nm^{-3}. (b),(d) Cu_2O/PbS nanoparticle surplus charge-induced relative change of symmetric mode's linewidth (black dash-dotted line), dip value (red solid line), and mode splitting (blue dashed line) with respect to the neutral case, for different n_b. Other parameters are the Cu_2O/PbS nanoparticle radius $r = 40$ nm and the cavity quality factor $Q \sim 10^8$.

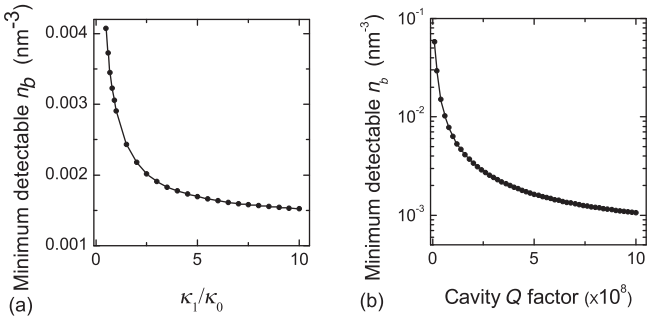

FIG. 7. Minimum detectable n_b of Cu_2O nanoparticle under different (a) κ_1/κ_0 (cavity $Q = 5 \times 10^8$, nanoparticle radius $r = 40$ nm);(b) cavity Q factors (nanoparticle radius $r = 40$ nm, $\kappa_1/\kappa_0 = 6.0$).

Cu_2O nanoparticle. Other nanoparticles such as PbS can be discussed similarly. We plot the minimum detectable bulk electron density under different parameters including κ_1/κ_0 and cavity Q factor in Fig. 7. A lower detection limit can be achieved with the increase of κ_1/κ_0 and cavity Q factor. For example, when $Q = 5 \times 10^8$, $\kappa_1/\kappa_0 = 6$, and $r = 40$ nm, the detection limit is $n_b = 0.001\,64$ nm^{-3}. Moreover, under a wide range of κ_1/κ_0 and cavity Q factor, bulk electron density as low as $n_b = 0.002$ nm^{-3} can be detected.

IV. DISCUSSION AND CONCLUSION

For simplicity, we have set the radius of the microsphere to be $R = 15$ μm throughout the paper. For a larger microsphere with $R = 25$ μm, the minimum detectable $n_s = 0.015$ nm^{-2}. In an actual sensing application, the microcavity radius can be optimized because of the tradeoff between the quality factor and the evanescent field fraction. For instance, with the increase of R, a higher quality factor can be obtained, while the fraction of evanescent field that benefits the nanoparticle detection reduces. As a result, an optimum R exists at which the best detection limit can be achieved.

The sensing signal should be strong enough for the scheme to be realized experimentally. Here, we discuss the signal intensity. For example, the charge-induced relative and absolute changes of the mode coupling depth are as large as 25% and 0.0675 for an MgO nanoparticle with charge density $n_s = 0.3$ nm^{-2} [Fig. 3(b)]. In the experiment, the fiber-microcavity coupling can be kept quite stable with instability <0.01. As a result, such a large change of the transmission spectrum can be recognized easily. By using a high-index prism, the microcavity coupling could be even more stable [69]. The relative and absolute changes of coupling depth for a much lower charge density of $n_s = 0.1$ nm^{-2} are 5% and 0.0135, both of which are also detectable with a reasonable signal-to-noise ratio. For the case of a LiF nanoparticle, the charge-induced change of coupling depth is even more prominent [Fig. 3(d)].

Moreover, the effects imposed by various turbulances such as material impurities should be differentiated from that by charge. Taking the MgO nanoparticle as an example, we compare the transmission spectrum of the microcavity under the adsorption of three cases: a neutral pure MgO nanoparticle, a charged pure MgO nanoparticle, and a neutral MgO nanoparticle with impurity. As the asymmetric mode is not affected, here we only show the symmetric mode. The result is shown in Fig. 8. Either for a very small change of refractive index ($\Delta n = 0.01$) induced by the material impurity or for a relatively large change ($\Delta n = 0.1$), the impurity mainly causes the change of mode splitting, whereas the surplus charge mainly leads to the change of dip value. We can differentiate the effects brought by the material impurities and by surplus charge from the transmission spectrum. For nanoparticles with $\chi < 0$, the effects induced by surplus charge can be easily differentiated from that caused by impurities. However, for nanoparticles with $\chi > 0$, special attention should be paid when the impurities reduce the refractive index. At this case, the effect caused by surplus charge and that by the impurities could not be distinguished just from the transmission spectrum because they both lead to blueshift. Additional tests (such as magnetic bias) are needed to distinguish charge from impurities.

It should be noticed that our methods are not limited to the above-mentioned materials including MgO, LiF, PbS,

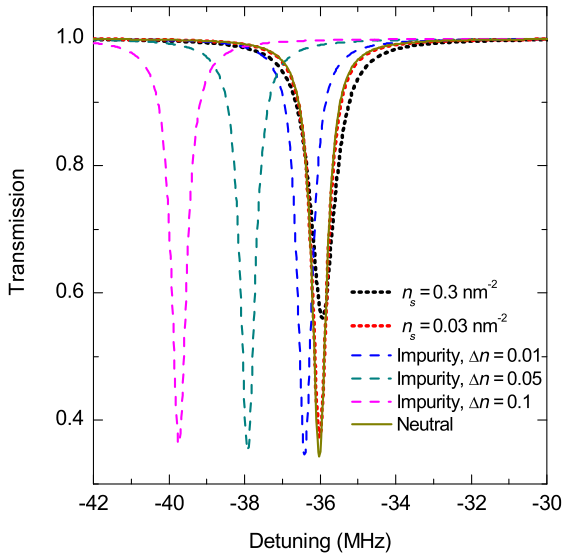

FIG. 8. Transmission spectrum for a WGM microcavity with a single deposited pure neutral MgO nanoparticle (black solid curve), pure MgO nanoparticle with charge density $n_s = 0.03$ nm^{-2} (red dotted curve), $n_s = 0.3$ nm^{-2} (blue dotted curve) and a neutral MgO nanoparticle with impurity-induced refractive-index change $\Delta n = 0.01$ (purple solid curve), 0.05 (green solid curve), 0.1 (blue solid curve). Other parameters: the nanoparticle radius $r = 40$ nm, cavity quality factor $Q \sim 5 \times 10^8$, and $\kappa_1/\kappa_0 = 1$.

Cu_2O, and Al_2O_3. The reason why we choose those materials as a model is that their parameters are accessible and they are important in the research area of charged nanoparticles. It is easy to extend our formulation to other materials, but the details such as material parameters, and the memory function, are different.

In summary, we propose to detect the charge of a single dielectric nanoparticle by monitoring the transmission spectrum of a WGM microcavity. The nanoparticle charge leads to obvious changes of the transmission spectrum compared with a neutral nanoparticle case. When a single neutral nanoparticle enters the mode volume of the WGM microcavity, the originally degenerate CW and CCW whispering gallery modes will split into two new modes: the symmetric and asymmetric modes. For a nanoparticle with negative electron affinity $\chi < 0$, the transmission dip value and the linewidth of the symmetric mode change obviously, while the mode splitting rarely changes. However, for a nanoparticle with positive electron affinity $\chi > 0$, the mode-splitting change is dominant. As a result, for $\chi < 0$ nanoparticles such as MgO and LiF, we can first use the mode splitting to determine the particle size, and then use the dip value or the linewidth to measure the charge, with the detection limit down to $n_s \sim 0.007$ nm^{-2}; while for $\chi > 0$ nanoparticles such as PbS, Cu_2O, and Al_2O_3, we can first use the dip value or the linewidth to get the information about the particle size, and then use the mode splitting for the determination of charge, with the detection limit down to $n_b \sim 0.001$ nm^{-3}. This high-Q optical microresonator-based nanoparticle charge measuring scheme has many advantages: it is independent of the unknown plasma parameters [70]; it is easy to be realized experimentally, without complicated surface treatment and nonlinear optical manipulation [38]; and the sensitivity is so high that surplus charge with very low charge density can be detected.

ACKNOWLEDGMENTS

This work is supported by National Science Foundation of China (No. 61377068, No. 61435001, and No. 11474011), Research Grants Council (RGC) of Hong Kong (N_PolyU505/13, PolyU 5334/12E, and PolyU 152184/15E), and The Hong Kong Polytechnic University (G-YN07, G-YBBE, 1-ZVAW, 4-BCAL, 1-ZE14, and A-PM21).

[1] F. Vollmer, D. Braun, A. Libchaber, M. Khoshsima, I. Teraoka, and S. Arnold, Protein detection by optical shift of a resonant microcavity, Appl. Phys. Lett. **80**, 4057 (2002).

[2] N. M. Hanumegowda, C. J. Stica, B. C. Patel, I. White, and X. Fan, Refractometric sensors based on microsphere resonators, Appl. Phys. Lett. **87**, 201107 (2005).

[3] S. Avino, A. Krause, R. Zullo, A. Giorgini, P. Malara, P. De Natale, H. P. Loock, and G. Gagliardi, Direct sensing in liquids using whispering-gallery-mode droplet resonators, Adv. Opt. Mater. **2**, 1155 (2014).

[4] C.-Y. Chao, W. Fung, and L. J. Guo, Polymer microring resonators for biochemical sensing applications, IEEE J. Sel. Top. Quantum Electron. **12**, 134 (2006).

[5] H. Zhu, I. M. White, J. D. Suter, P. S. Dale, and X. Fan, Analysis of biomolecule detection with optofluidic ring resonator sensors, Opt. Express **15**, 9139 (2007).

[6] M. Sumetsky, R. S. Windeler, Y. Dulashko, and X. Fan, Optical liquid ring resonator sensor, Opt. Express **15**, 14376 (2007).

[7] A. L. Washburn, L. C. Gunn, and R. C. Bailey, Label-free quantitation of a cancer biomarker in complex media using silicon photonic microring resonators, Anal. Chem. **81**, 9499 (2009).

[8] S. Lin and K. B. Crozier, Planar silicon microrings as wavelength-multiplexed optical traps for storing and sensing particles, Lab Chip **11**, 4047 (2011).

[9] B.-Q. Shen, X.-C. Yu, Y. Zhi, L. Wang, D. Kim, Q. Gong, and Y.-F. Xiao, Detection of Single Nanoparticles Using the Dissipative Interaction in a High-Q Microcavity, Phys. Rev. Applied **5**, 024011 (2016).

[10] A. M. Armani and K. J. Vahala, Heavy water detection using ultra-high-Q microcavities, Opt. Lett. **31**, 1896 (2006).

[11] X. Zhang and A. M. Armani, Silica microtoroid resonator sensor with monolithically integrated waveguides, Opt. Express **21**, 23592 (2013).

[12] S. Rosenblum, Y. Lovsky, L. Arazi, F. Vollmer, and B. Dayan, Cavity ring-up spectroscopy for ultrafast sensing with optical microresonators, Nat. Commun. **6**, 6788 (2015).

[13] M. Sumetsky, Y. Dulashko, and R. S. Windeler, Optical microbubble resonator, Opt. Lett. **35**, 898 (2010).

[14] Y. Yang, J. Ward, and S. N. Chormaic, Quasi-droplet microbubbles for high resolution sensing applications, Opt. Express **22**, 6881 (2014).

[15] M. Li, X. Wu, L. Liu, X. Fan, and L. Xu, Self-referencing optofluidic ring resonator sensor for highly sensitive biomolecular detection, Anal. Chem. **85**, 9328 (2013).

[16] L. Ma, S. Li, V. A. Bolaños Quiñones, L. Yang, W. Xi, M. Jorgensen, S. Baunack, Y. Mei, S. Kiravittaya, and O. G. Schmidt, Dynamic molecular processes detected by microtubular opto-chemical sensors self-assembled from prestrained nanomembranes, Adv. Mater. **25**, 2357 (2013).

[17] S. Li, L. Ma, S. Böttner, Y. Mei, M. R. Jorgensen, S. Kiravittaya, and O. G. Schmidt, Angular position detection of single nanoparticles on rolled-up optical microcavities with lifted degeneracy, Phys. Rev. A **88**, 033833 (2013).

[18] M. R. Foreman, J. D. Swaim, and F. Vollmer, Whispering gallery mode sensors, Adv. Opt. Photonics **7**, 168 (2015).

[19] X. Fan, I. M. White, S. I. Shopova, H. Zhu, J. D. Suter, and Y. Sun, Sensitive optical biosensors for unlabeled targets: A review, Anal. Chim. Acta **620**, 8 (2008).

[20] F. Vollmer and S. Arnold, Whispering-gallery-mode biosensing: Label-free detection down to single molecules, Nat. Methods **5**, 591 (2008).

[21] S. Arnold, M. Khoshsima, I. Teraoka, S. Holler, and F. Vollmer, Shift of whispering-gallery modes in microspheres by protein adsorption, Opt. Lett. **28**, 272 (2003).

[22] F. Vollmer, S. Arnold, and D. Keng, Single virus detection from the reactive shift of a whispering-gallery mode, Proc. Natl. Acad. Sci. U.S.A. **105**, 20701 (2008).

[23] W. Weng, J. D. Anstie, and A. Luiten, Refractometry with Ultralow Detection Limit Using Anisotropic Whispering-Gallery-Mode Resonators, Phys. Rev. Applied **3**, 044015 (2015).

[24] T. Lu, H. Lee, T. Chen, S. Herchak, J.-H. Kim, S. E. Fraser, R. C. Flagan, and K. Vahala, High sensitivity nanoparticle detection using optical microcavities, Proc. Natl. Acad. Sci. U.S.A. **108**, 5976 (2011).

[25] V. R. Dantham, S. Holler, Z. Wan, V. Kolchenko, and S. Arnold, Taking whispering gallery mode single virus detection and sizing to the limit, Appl. Phys. Lett. **101**, 043704 (2012).

[26] J. D. Swaim, J. Knittel, and W. P. Bowen, Detection of nanoparticles with a frequency locked whispering gallery mode microresonator, Appl. Phys. Lett. **102**, 183106 (2013).

[27] J. Zhu, S. K. Özdemir, Y.-F. Xiao, L. Li, L. He, D.-R. Chen, and L. Yang, On-chip single nanoparticle detection and sizing by mode splitting in an ultrahigh-Q microresonator, Nat. Photonics **4**, 46 (2010).

[28] A. Mazzei, S. Götzinger, L. de S. Menezes, G. Zumofen, O. Benson, and V. Sandoghdar, Controlled Coupling of Counterpropagating Whispering-Gallery Modes by a Single Rayleigh Scatterer: A Classical Problem in a Quantum Optical Light, Phys. Rev. Lett. **99**, 173603 (2007).

[29] B.-B. Li, W. R. Clements, X.-C. Yu, K. Shi, Q. Gong, and Y.-F. Xiao, Single nanoparticle detection using split-mode microcavity Raman lasers, Proc. Natl. Acad. Sci. U.S.A. **111**, 14657 (2014).

[30] S. K. Özdemir, J. Zhu, X. Yang, B. Peng, H. Yilmaz, L. He, F. Monifi, G. L. Long, and L. Yang, Highly sensitive detection of nanoparticles with a self-referenced and self-heterodyned whispering-gallery Raman microlaser, Proc. Natl. Acad. Sci. U.S.A. **111**, E3836 (2014).

[31] L. Shao, X.-F. Jiang, X.-C. Yu, B.-B. Li, W. R. Clements, F. Vollmer, W. Wang, Y.-F. Xiao, and Q. Gong, Detection of single nanoparticles and lentiviruses using microcavity resonance broadening, Adv. Mater. **25**, 5616 (2013).

[32] Y. Hu, L. Shao, S. Arnold, Y.-C. Liu, C.-Y. Ma, and Y.-F. Xiao, Mode broadening induced by nanoparticles in an optical whispering-gallery microcavity, Phys. Rev. A **90**, 043847 (2014).

[33] J. E. Dyson and D. A. Williams, *The Physics of the Interstellar Medium*, 2nd ed. (Institute of Physics Publishing, Bristol and Philadelphia, 1997).

[34] J. J. Wu and R. J. Miller, Measurements of charge on submicron particles generated in a sputtering process, J. Appl. Phys. **67**, 1051 (1990).

[35] T. Trottenberg, A. Melzer, and A. Piel, Measurement of the electric charge on particulates forming Coulomb crystals in the sheath of a radiofrequency plasma, Plasma Sources Sci. Technol. **4**, 450 (1995).

[36] D. Mendis, Progress in the study of dusty plasmas, Plasma Sources Sci. Technol. **11**, A219 (2002).

[37] M.-C. Daniel, I. B. Tsvetkova, Z. T. Quinkert, A. Murali, M. De, V. M. Rotello, C. Cheng Kao, and B. Dragnea, Role of surface charge density in nanoparticle-templated assembly of bromovirus protein cages, ACS Nano **4**, 3853 (2010).

[38] R. R. Kumal, T. E. Karam, and L. H. Haber, Determination of the surface charge density of colloidal gold nanoparticles using second harmonic generation, J. Phys. Chem. C **119**, 16200 (2015).

[39] C. F. Bohren and A. J. Hunt, Scattering of electromagnetic waves by a charged sphere, Can. J. Phys. **55**, 1930 (1977).

[40] J. Klačka and M. Kocifaj, On the scattering of electromagnetic waves by a charged sphere, Prog. Electromagn. Res. **109**, 17 (2010).

[41] M. Kocifaj and J. Klačka, Scattering of electromagnetic waves by charged spheres, Opt. Lett. **37**, 265 (2012).

[42] R. L. Heinisch, F. X. Bronold, and H. Fehske, Mie Scattering by a Charged Dielectric Particle, Phys. Rev. Lett. **109**, 243903 (2012).

[43] R. L. Heinisch, F. X. Bronold, and H. Fehske, Optical signatures of the charge of a dielectric particle in a plasma, Phys. Rev. E **88**, 023109 (2013).

[44] E. Thiessen, R. L. Heinisch, F. X. Bronolda, and H. Fehske, Infrared light extinction by charged dielectric core-coat particles, Eur. Phys. J. D **68**, 98 (2014).

[45] J. Klačka, M. Kocifaj, F. Kundracik, G. Videen, and I. Kohút, Generalization of electromagnetic scattering by charged grains through incorporation of interband and intraband effects, Opt. Lett. **40**, 5070 (2015).

[46] E. Sijercica and P. T. Leungb, Effects of surface charge on the anomalous light extinction from metallic nanoparticles, Opt. Commun. **370**, 198 (2016).

[47] E. Rosenkrantz and S. Arnon, Enhanced absorption of light by charged nanoparticles, Opt. Lett. **35**, 1178 (2010).

[48] N. Wang, S. Liu, and Z. Lin, Tailoring optical properties of surface charged dielectric nanoparticles based on an effective medium theory, Opt. Express **21**, 20387 (2013).

[49] H. Y. Chung, P. T. Leung, and D. P. Tsai, Effects of extraneous surface charges on the enhanced Raman scattering from metallic nanoparticles, J. Chem. Phys. **138**, 224101 (2013).

[50] H. Y. Chung, P. T. Leung, and D. P. Tsai, Molecular fluorescence in the vicinity of a charged metallic nanoparticle, Opt. Express **21**, 26483 (2013).

[51] J. T. Kim, S. Spindler, and V. Sandoghdar, Scanning-aperture trapping and manipulation of single charged nanoparticles, Nat. Commun. **5**, 3380 (2014).

[52] H. Ikezi, Coulomb solid of small particles in plasmas, Phys. Fluids **29**, 1764 (1986).

[53] J. E. Allen, Probe theory—The orbital motion approach, Phys. Scr. **45**, 497 (1992).

[54] B. Walch, M. Horanyi, and S. Robertson, Measurement of the charging of individual dust grains in a plasma, IEEE Trans. Plasma Sci. **22**, 97 (1994).

[55] D. S. Weiss, V. Sandoghdar, J. Hare, V. Lefèvre-Seguin, J.-M. Raimond, and S. Haroche, Splitting of high-Q Mie modes induced by light backscattering in silica microspheres, Opt. Lett. **20**, 1835 (1995).

[56] B. E. Little, J.-P. Laine, and S. T. Chu, Surface-roughness-induced contradirectional coupling in ring and disk resonators, Opt. Lett. **22**, 4 (1997).

[57] M. L. Gorodetsky, A. D. Pryamikov, and V. S. Tlchenko, Rayleigh scattering in high-Q microspheres, J. Opt. Soc. Am. B **17**, 1051 (2000).

[58] J. Kippenberg, S. M. Spillane, and K. J. Vahala, Modal coupling in traveling-wave resonators, Opt. Lett. **27**, 1669 (2002).

[59] M. Borselli, T. Johnson, and O. Painter, Beyond the Rayleigh scattering limit in high-Q silicon microdisks: Theory and experiment, Opt. Express **13**, 1515 (2005).

[60] R. L. Heinisch, F. X. Bronold, and H. Fehske, Electron surface layer at the interface of a plasma and a dielectric wall, Phys. Rev. B **85**, 075323 (2012).

[61] M. Rohlfing, N.-P. Wang, P. Krüger, and J. Pollmann, Image States and Excitons at Insulator Surfaces with Negative Electron Affinity, Phys. Rev. Lett. **91**, 256802 (2003).

[62] W. Götze and P. Wölfle, Homogeneous dynamical conductivity of simple metals, Phys. Rev. B **6**, 1226 (1972).

[63] C. F. Bohren and D. R. Huffman, *Absorption and scattering of light by small particles* (Wily, New York, 1983).

[64] X. Yi, Y.-F. Xiao, Y.-C. Liu, B.-B. Li, Y.-L. Chen, Y. Li, and Q. Gong, Multiple-Rayleigh-scatterer-induced mode splitting in a high-Q whispering-gallery-mode microresonator, Phys. Rev. A **83**, 023803 (2011).

[65] Y. Li and X. Fan, Microring resonators with flow-through nanopores for nanoparticle counting and sizing, Opt. Express **21**, 229 (2013).

[66] M. R. Foreman, W.-L. Jin, and F. Vollmer, Optimizing detection limits in whispering gallery mode biosensing, Opt. Express **22**, 5491 (2014).

[67] A. B. Matsko, A. A. Savchenkov, N. Yu, and L. Maleki, Whispering-gallery-mode resonators as frequency references. I. Fundamental limitations, J. Opt. Soc. Am. B **24**, 1324 (2007).

[68] M. L. Gorodetsky and I. S. Grudinin, Fundamental thermal fluctuations in microspheres, J. Opt. Soc. Am. B **21**, 697 (2004).

[69] M. D. Baaske, M. R. Foreman, and F. Vollmer, Single-molecule nucleic acid interactions monitored on a label-free microcavity biosensor platform, Nat. Nanotechnol. **9**, 933 (2014).

[70] J. Carstensen, H. Jung, F. Greiner, and A. Piel, Mass changes of microparticles in a plasma observed by a phase-resolved resonance method, Phys. Plasmas **18**, 033701 (2011).